Fe$_2$O$_3$ nanorods/carbon nanofibers composite: Preparation and performance as anode of high rate lithium ion battery

CrossMark

Chunyu Wu [a], Xiaoping Li [a,b,c], Weishan Li [a,b,c,*], Bin Li [a], Yaqiong Wang [a], Yating Wang [a], Mengqing Xu [a,b,c], Lidan Xing [a,b,c]

[a] School of Chemistry and Environment, South China Normal University, Guangzhou 510006, China
[b] Key Laboratory of Electrochemical Technology on Energy Storage and Power Generation of Guangdong Higher Education Institutes, South China Normal University, Guangzhou 510006, China
[c] Engineering Research Center of Materials and Technology for Electrochemical Energy Storage, Ministry of Education, South China Normal University, Guangzhou 510006, China

H I G H L I G H T S

- Novel α-Fe$_2$O$_3$ nanorods/carbon nanofibres composite is prepared hydrothermally with PVP-assistance.
- α-Fe$_2$O$_3$ nanorods are enwrapped with soft and curly carbon nanofibers.
- Composite exhibits superior performance in terms of rate capability and cycle stability.
- Bondage from the nanofibres improves electronic conductivity and structure stability of α-Fe$_2$O$_3$.

A R T I C L E   I N F O

A B S T R A C T

A novel Fe$_2$O$_3$/carbon composite is prepared using a facile one-step hydrothermal method. Its structure, morphology and performance as anode of lithium ion battery are investigated with X-ray diffraction, scanning electron microscopy, thermogravimetry, cyclic voltammetry, galvanostatic charge/discharge, and electrochemical impedance spectroscopy. It is found that the as-prepared composite is composed of α-Fe$_2$O$_3$ nanorods of about 75 nm in diameter and 1 μm in length, which are enwrapped with soft and curly carbon nanofibers, and exhibits superior charge/discharge performance compared to bare α-Fe$_2$O$_3$ nanorods, especially at high current rate. The discharge capacity is 1069 mAh g^{-1} at the first cycle and remains 560 mAh g^{-1} after 30 cycles at 0.2C for the bare nanorods, but improved to 1278 mAh g^{-1} and 960 mAh g^{-1} for the composite. At 12C, the discharge capacity is only 798 mAh g^{-1} initially and becomes 98 mAh g^{-1} after 30 cycles for the bare nanorods, while 844 mAh g^{-1} and 292 mAh g^{-1} for the composite. The improved performance of the composite is attributed to the bondage from carbon nanofibers, which contributes to the improvement in electronic conductivity and structure stability of α-Fe$_2$O$_3$ nanorods.

1. Introduction

Electrochemical energy storage is becoming increasingly important due to the exploitation of solar and wind energy and the application of electric vehicles [1,2]. Compared to other electrochemical energy storage systems, lithium ion battery (LIB) exhibits high energy density and has been widely used in portable electronic devices, but its performance needs to be improved for the applications in large scale [3,4]. Due to the variety of electrode materials, there is much room for the performance improvement of current LIB. Substituting transition metal oxides for graphite anode is one of the strategies for improving the energy density of LIB [5–7]. α-Fe$_2$O$_3$ has attracted considerable attention because of its high theoretical capacity (1007 mAh g^{-1}) compared to graphite (372 mAh g^{-1}), eco-friendliness and natural abundance. Unfortunately, α-Fe$_2$O$_3$ has its limits, including vast volume inflation (over 200%) and poor electrical conductivity [8].
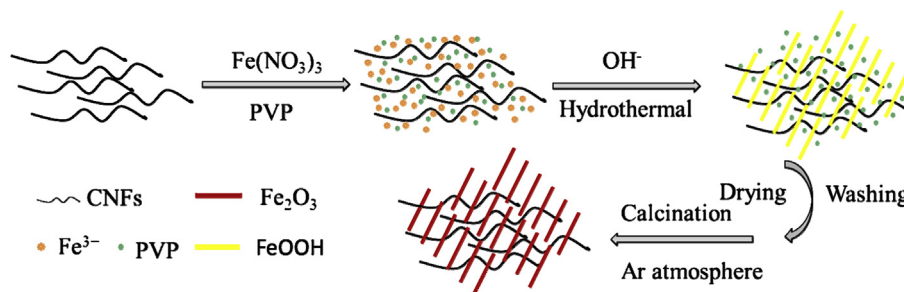
Scheme 1. Schematic preparation process of α-Fe$_2$O$_3$ nanorods/CNFs.

Many nanostructured materials, such as 0D (nanoparticles), 1D (nanorods, nanowires and nanotubes), 2D/3D (nanorings, nanobelts, nanocubes, as well as hollow and porous nanostructures), have been designed to reduce the structure instability resulting from volume inflation [9,10]. However, the large surface area of nanostructured materials usually yields side-reactions such as the dissolution of anode materials and the degradation of electrolyte. To solve the problem above-mentioned, many carbon composites, such as α-Fe$_2$O$_3$/graphene [11], α-Fe$_2$O$_3$ nanoparticle/carbon aerogel [12], α-Fe$_2$O$_3$/CNTs [13], α-Fe$_2$O$_3$/graphene aerogel [14], α-Fe$_2$O$_3$/SWNTs [15], α-Fe$_2$O$_3$/MWCNTs [16], α-Fe$_2$O$_3$/CNSs [17], and carbon-coating α-Fe$_2$O$_3$ [18], have been developed. For example, α-Fe$_2$O$_3$ nanorods array on electrospinning carbon nanofibers (CNFs) exhibits good rate capability and cycle stability as anode of lithium ion battery [19,20]. The carbon in the composite not only prevents the side-reactions on the active materials, but also provides a conductive network to improve the electrical conductivity of anode materials [21—23].

In this paper, we reported a novel α-Fe$_2$O$_3$/carbon composite. α-Fe$_2$O$_3$ nanorods were formed by hydrothermal method with polyvinylpyrrolidone (PVP) as dispersant, and soft and curly carbon nanofibers (CNFs) were introduced during the formation of α-Fe$_2$O$_3$ nanorods, resulting in α-Fe$_2$O$_3$ nanorods/CNFs composite, as shown in Scheme 1. The resulting composite is expected to exhibit superior electrochemical performance because of the integration of several advantageous structural features. Firstly, the 1D α-Fe$_2$O$_3$ nanorods provide a large surface area and large surface to volume ratio, thus leading to relatively short ion and charge diffusion pathways and high transport rates of both lithium ions and electrons. Secondly, the highly conductive CNFs provide an electronic network to facilitate the charge transfer [24]. Thirdly, the soft and curly CNFs enwrap the α-Fe$_2$O$_3$ nanorods preventing the nanostructure from pulverization during cycling.

2. Experimental

2.1. Preparation of α-Fe$_2$O$_3$ nanorods/CNFs

Typically, 0.2 g PVP and 50 mg carbon nanofibers (200 nm in diameter and 50 μm in length, Sigma—Aldrich) were dispersed in the mixed solution of 40 ml ethyl alcohol and 40 ml deionized water under strongly stirring, 4.04 g Fe(NO$_3$)$_3$·9H$_2$O was added forming a yellow solution and then 0.16 g NaOH was slowly added forming a brown solution. The resulting solution was transferred into a sealed Teflon-lined stainless steel autoclave (100 ml) and heated to 120 °C for 12 h. After cooling down to room temperature naturally, the precursor (α-FeOOH nanorods/CNFs) was filtered, washed with absolute ethanol and distilled water several times to remove the solvent effectively, and then dried in an oven at 60 °C overnight. Finally, the dried powers were further calcined at 350 °C for 3 h in a flowing nitrogen (N$_2$) atmosphere, and α-Fe$_2$O$_3$

nanorods/CNFs composite was obtained. Bare α-Fe$_2$O$_3$ nanorods were prepared for comparison by the same hydrothermal synthesis without adding carbon nanofibers.

2.2. Electrochemical measurements

Electrochemical measurements were conducted by using a half coin-type cell (CR2025) assembled in a glove box (MBraun, Germany) under an argon atmosphere at room temperature (25 °C). The working electrode was fabricated by mixing the 80 wt% active material (α-Fe$_2$O$_3$ nanorods/CNFs or bare α-Fe$_2$O$_3$ nanorods), 10 wt % acetylene black and 10 wt% polyvinylidene fluoride (PVDF) binder, coating the mixture on the copper current collector with 10 μm thick and drying at 120 °C in a vacuum oven for 12 h. Metallic lithium foil was used as the counter electrode, 1 M LiPF$_6$ in ethylene carbonate (EC) and dimethyl carbonate (DMC) (EC:DMC = 1:1 in volume) as the electrolyte and a polypropylene microporous film (Cellgard 2300) as the separator. The galvanostatic charge/discharge tests were performed on LAND CT 2001A (China) battery testing system at different current rates in a voltage range from 0.005 to 3.0 V (vs. Li$^+$/Li). The cyclic voltammetry (CV) was performed on Solartron Analytical 1470E Cell Test System (England) in the range of 0.005—3.0 V (vs. Li$^+$/Li) with a scan rate of 0.1 mV s^{-1}. Electrochemical impedance spectroscopy (EIS) was performed on fresh cells at open circuit potential with Auto lab (PGSTAT-30, Eco Echemie B.V. Company) by applying a sine wave with voltage amplitude of 5.0 mV over the frequency range from 100 kHz to 0.01 Hz.
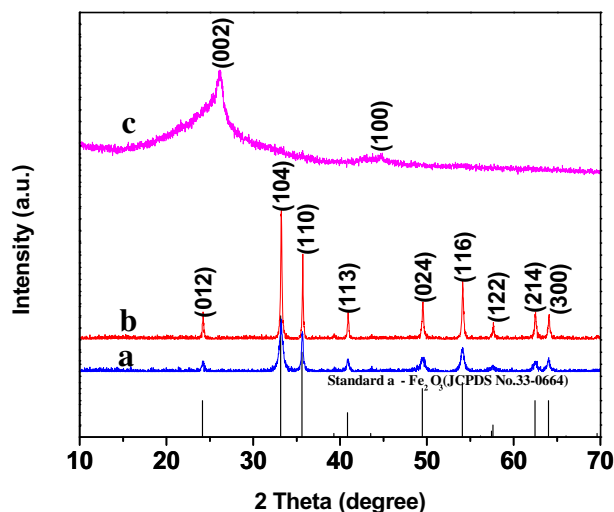
Fig. 1. Wide-angle XRD pattern of bare α-Fe$_2$O$_3$ nanorods (a), α-Fe$_2$O$_3$ nanorods/CNFs (b) and bare CNFs (c), together with standard card of α-Fe$_2$O$_3$ (JCPDS no. 33-0664).

2.3. Materials characterization

The morphology of the samples were observed by scanning electron microscopy (SEM; Zelss Ultra 55, Germany), which was operated at 200 kV. The crystallographic information for the samples was examined by X-ray power diffraction (XRD) recorded on a powder diffractometer (Bruker D8 Advanced Diffractometer System) with Cu-Kα radiation ($\lambda = 0.154056$ nm) source. The thermogravimetric analysis (TGA) was performed under an air flow of 100 mL min^{-1} using Du Pont Instruments TGA 2950 from room temperature to 800 °C with a heating rate of 10 °C min^{-1}.

3. Results and discussion

3.1. Structure and morphology

The power XRD pattern provides crystalline and phase information of the examined samples. Fig. 1 presents the XRD patterns of the resulting samples together with the standard card of α-Fe$_2$O$_3$.

Curve a in Fig. 1 is the XRD pattern of bare Fe$_2$O$_3$ sample. There are the nine characteristic diffraction peaks located at 24.1°, 33.1°, 35.6°, 40.8°, 49.5°, 54.1°, 57.6°, 62.4° and 64.0°, which are matched well with the (0 1 2), (1 0 4), (1 1 0), (1 1 3), (0 2 4), (1 1 6), (1 2 2), (2 1 4) and (3 0 0) crystal planes of α-Fe$_2$O$_3$ (JCPDS no. 33-0664). Therefore, the resulting sample is α-Fe$_2$O$_3$. Curve c in Fig. 1 is the XRD pattern of carbon nanofibers, which have two broad diffraction peaks at ca. 26.2° and 44.8°, corresponding to the (0 0 2) and (1 0 0) reflections of carbon, respectively. Curve b is the XRD pattern of the composite, which has a similar diffraction to bare α-Fe$_2$O$_3$ and shows that the introduction of carbon nanofibers does not change the crystal structure of α-Fe$_2$O$_3$. No carbon signals were observed, this is because the content of carbon nanofibers in the sample is too low (5 wt%, estimated from TGA). The intense peaks of the XRD pattern are indicative of the well crystallinity of the product and no any other impurity peaks confirm the high purity of the products. The XRD matching results show that the lattice parameter values are $a = 5.037$ Å, 5.039 Å and $c = 13.771$ Å, 13.770 Å, for the bare α-Fe$_2$O$_3$ and the composite, respectively.
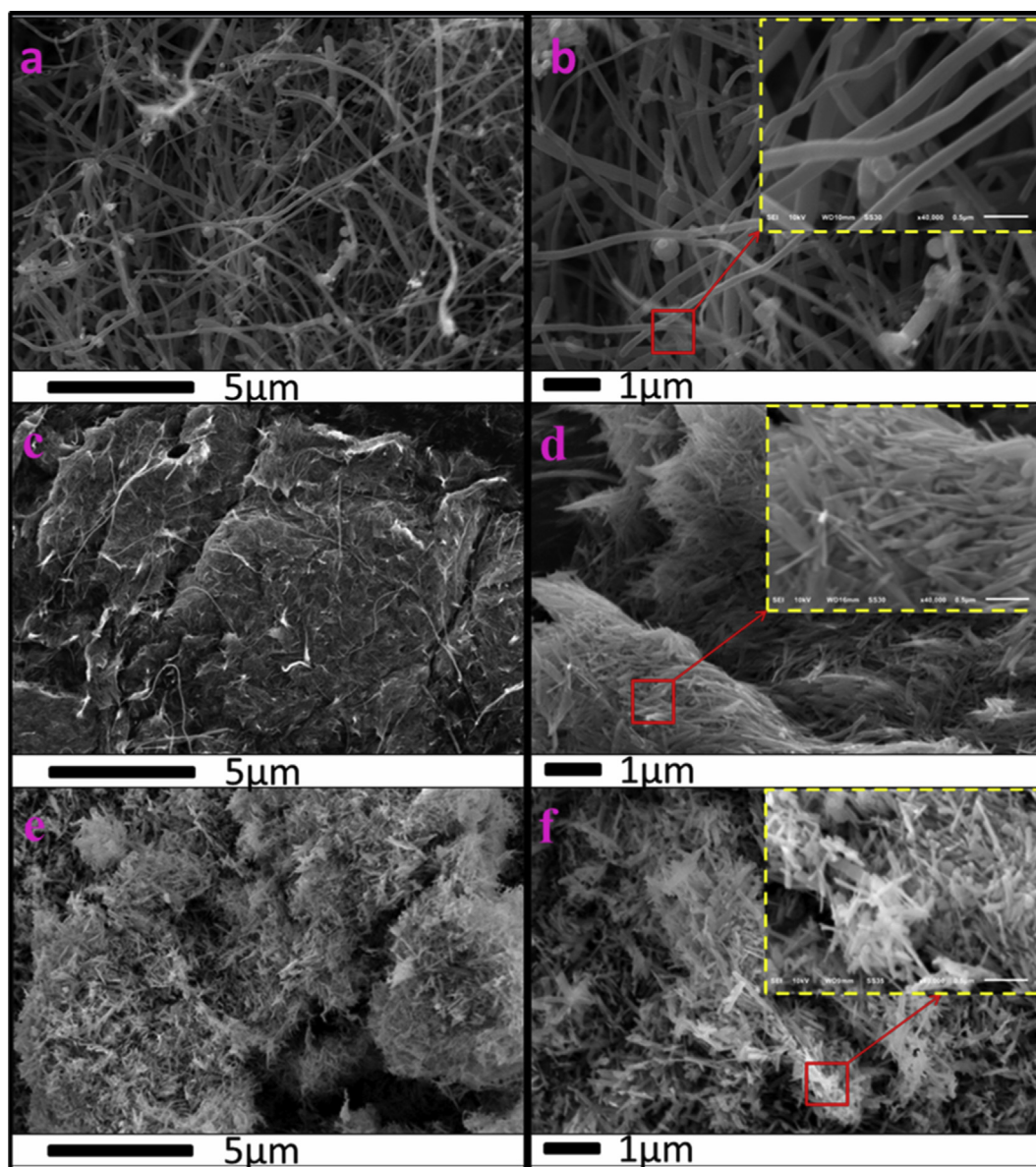

Fig. 2. SEM images of bare CNFs (a, b), α-Fe$_2$O$_3$ nanorods/CNFs (c, d) and bare α-Fe$_2$O$_3$ nanorods (e, f).

The morphology of the resulting samples was observed by SEM. Fig. 2 presents the observed results. As seen from Fig. 2a and b, carbon nanofibers can be well identified, which are soft and curly. It can be seen from Fig. 2c that the formed α-Fe$_2$O$_3$ nanorods are enwrapped by the curly carbon nanofibers. Fig. 2d shows that the α-Fe$_2$O$_3$ nanorods are about 75 nm in diameter and 1 μm in length. The similar SEM image of the bare α-Fe$_2$O$_3$ nanorods (Fig. 2e and f) to that of the composite shows that the introduction of carbon fibers does not change the morphology of the α-Fe$_2$O$_3$.

The CNFs content in the α-Fe$_2$O$_3$ nanorods/CNFs composite was estimated by TGA measurement. As seen in Fig. 3a, the overall TGA curve can be divided into three distinct stages, marked as A, B, C. The weight loss of 5 wt% occurred between 25 °C and 170 °C (Region A), which is attributed to residual solvent evaporation. A further weight loss of 2 wt% occurred above 170–365 °C (Region B), which may be due to the complete reduction of α-FeOOH to α-Fe$_2$O$_3$ and the removal of the crystalline water molecules. The weight loss ceases at the 365 °C from the TGA curve of the bare α-Fe$_2$O$_3$ nanorods. The obvious weight loss of CNFs between 365 and 650 °C (region C) should be attributed to the combustion of CNFs. From Fig. 3b, we can know that the content of CNFs in the α-Fe$_2$O$_3$ nanorods/CNFs composite is about 5 wt%.
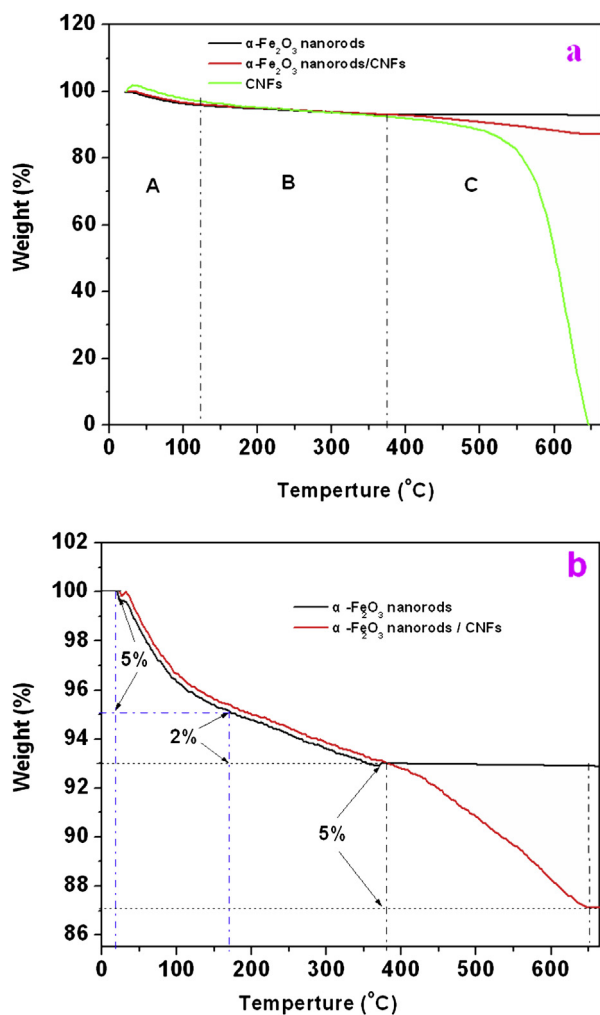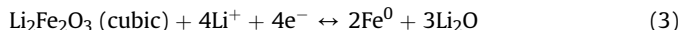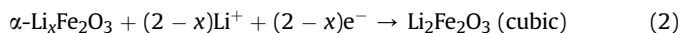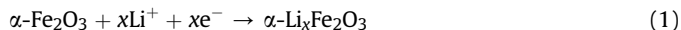
3.2. Electrochemical reversibility of lithium insertion/de-insertion

Fig. 4 presents the cyclic voltammograms of the α-Fe$_2$O$_3$ nanorods/CNFs and the bare α-Fe$_2$O$_3$ nanorods for the initial three cycles in the potential range of 0.05–3.0 V (vs. Li$^+$/Li) with a scan rate of 0.1 mV s^{-1}. As seen from Fig. 4a, in the first cycle there appear four peaks (A1, B1, C1 and D1) at 1.60, 0.94, 0.70 and 1.85 V, respectively, for the bare α-Fe$_2$O$_3$ nanorods, corresponding to the following lithium insertion/de-insertion processes [25]:

$$\alpha\text{-Fe}_2\text{O}_3 + x\text{Li}^+ + xe^- \rightarrow \alpha\text{-Li}_x\text{Fe}_2\text{O}_3 \tag{1}$$

$$\alpha\text{-Li}_x\text{Fe}_2\text{O}_3 + (2-x)\text{Li}^+ + (2-x)e^- \rightarrow \text{Li}_2\text{Fe}_2\text{O}_3 \text{ (cubic)} \tag{2}$$

$$\text{Li}_2\text{Fe}_2\text{O}_3 \text{ (cubic)} + 4\text{Li}^+ + 4e^- \leftrightarrow 2\text{Fe}^0 + 3\text{Li}_2\text{O} \tag{3}$$

The small reduction peak at around 1.60 V (A1) is attributed to the insertion of small amount of lithium into α-Fe$_2$O$_3$, which does not change its crystal structure (Eq. (1)) [26]. The second reduction peak at 0.94 V (B1) is attributed to the transformation of the hexagonal α-Li$_x$Fe$_2$O$_3$ to cubic Li$_2$Fe$_2$O$_3$. The big reduction peak at 0.70 V (C1) is corresponding to the complete reduction of Fe^{3+} and Fe^{2+} to Fe^0 which is accompanied with the formation of Li$_2$O [23,27]. The broad oxidation peak at about 1.85 V (D1) can be

Fig. 3. TGA curves of α-Fe$_2$O$_3$ nanorods/CNFs, bare α-Fe$_2$O$_3$ nanorods and bare CNFs in the weight region of 0–100% (a) and their magnification between 85 and 100% (b).
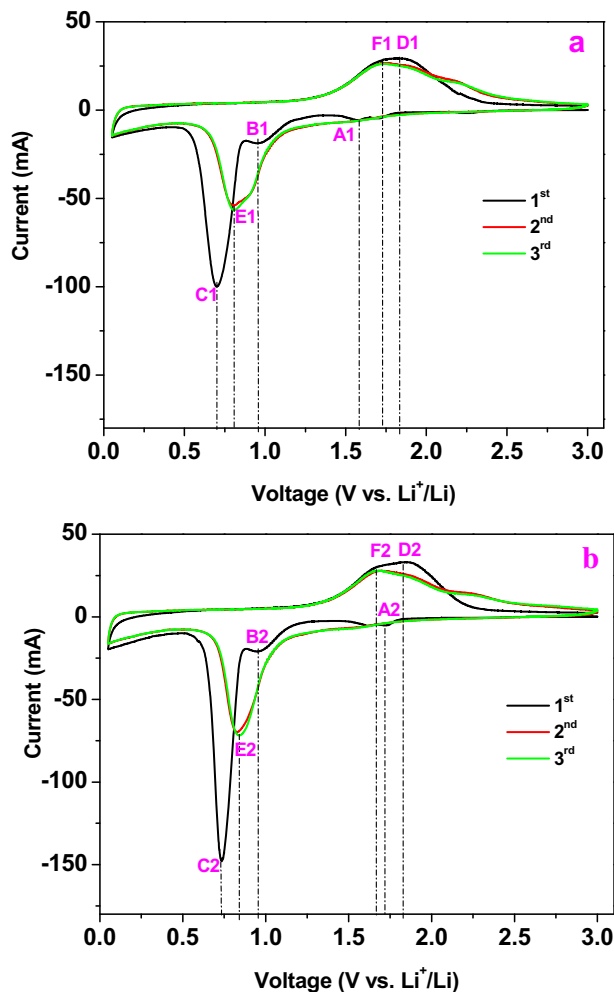
Fig. 4. Cyclic voltammograms of bare α-Fe$_2$O$_3$ nanorods (a) and α-Fe$_2$O$_3$ nanorods/ CNFs (b) electrodes at a scan rate of 0.1 mV s^{-1}.
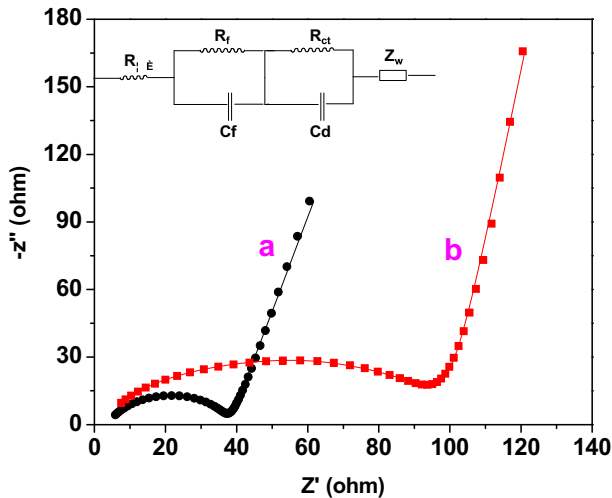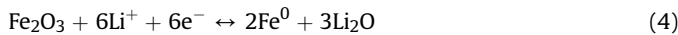
Fig. 5. AC impedance spectra of α-Fe$_2$O$_3$ nanorods/CNFs and α-Fe$_2$O$_3$ nanorods electrodes before cycling.

ascribed to the reversible oxidation of Fe^0 to Fe^{2+} and further oxidation to Fe^{3+}. The electrochemical reversible reaction can be summarized as [28]:

$$Fe_2O_3 + 6Li^+ + 6e^- \leftrightarrow 2Fe^0 + 3Li_2O \qquad (4)$$

If 6 mol of Li$^+$ were removed reversibly, a discharge capacity of 1007 mAh g^{-1} could be obtained [23]. Owing to the structural reorganization and new phase formation, the peaks of cathodic and anodic are distinctly shifted forming the new reduction peak at 0.81 V (E1) and the oxidation peak at 1.74 V (F1) in the subsequent cycles. The reduction peaks (A1 and B1) disappears from the second cycle, indicating that these reactions are irreversible.

Similar voltammetric behavior can be observed for α-Fe$_2$O$_3$ nanorods/CNFs, as shown in Fig. 4b, suggesting that the introduction of carbon nanofibres does not change the lithium insertion/de-insertion mechanism. However, the peak potentials are different. The corresponding peaks (A2, B2, C2, D2, E2, and F2) are located at 1.74, 0.96, 0.74, 1.82, 0.84, and 1.66 V, respectively. The reduction peak potentials shifts positively and the oxidation peak potentials negatively, suggesting that α-Fe$_2$O$_3$ nanorods/CNFs electrode has a faster lithium insertion/de-insertion kinetics than bare α-Fe$_2$O$_3$ nanorods electrode.

To confirm the improved lithium insertion/de-insertion kinetics of α-Fe$_2$O$_3$ nanorods due to the introduction of nanofibres, EIS measurements were performed on the α-Fe$_2$O$_3$ nanorods/CNFs and α-Fe$_2$O$_3$ nanorods electrodes and the obtained results are presented in Fig. 5 and Table 1. The inset of Fig. 5 is the equivalent circuit used to fit the experimental results. In this equivalent circuit, R_θ is the ohmic resistance related to electronic and ionic conductivity, C_f and R_f are the capacitance and the resistance of the surface film (usually composed of LiCO$_3$) between the interaction and the electrolyte, C_d and R_{ct} are the double-layer capacitance and the charge transfer resistance on the interface for lithium insertion/de-

insertion charge transfer step, Z_w reflects the diffusion difficulty of lithium ion in the inserted materials. The experimental results (dots) can be well fitted with the equivalent circuit (the solid lines is the fitted results with constant phase element as capacitor), indicating that the equivalent circuit can reflect the lithium insertion/de-insertion process. As shown in Table 1, all the resistance of the α-Fe$_2$O$_3$ nanorods/CNFs electrode is smaller than that of the bare α-Fe$_2$O$_3$ nanorods electrode, confirming the faster lithium insertion/de-insertion kinetics in the α-Fe$_2$O$_3$ nanorods/CNFs electrode. The introduction of CNFs into the α-Fe$_2$O$_3$ nanorods increases the electronic conductivity and thus reduces the ohmic resistance of the electrode. The inclusion of CNFs in α-Fe$_2$O$_3$ nanorods induces the contact between α-Fe$_2$O$_3$ and electrolyte and thus reduces the charge transfer resistance and the diffusion resistance of lithium ion in the electrode [35]. Therefore, the improved rate performance of α-Fe$_2$O$_3$ nanorods/CNFs as anode of lithium ion battery can be expected.

3.3. Charge–discharge performance

Fig. 6 presents the charge–discharge voltage profiles obtained at a current density of 200 mA g^{-1} (0.2C). In the first cycle, the bare α-Fe$_2$O$_3$ nanorods and the α-Fe$_2$O$_3$ nanorods/CNFs electrodes behaves similarly, the voltage plateaus can be observed, which is characteristic of transition-metal oxides [29–32]. However, the initial
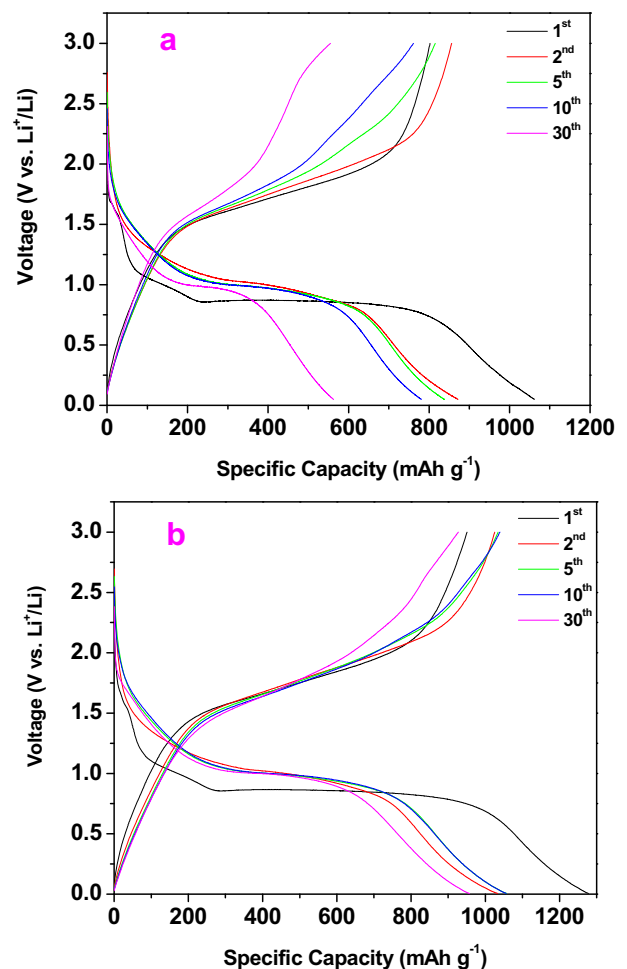
Table 1
Impedance parameters of the α-Fe$_2$O$_3$ nanorods/CNFs and the α-Fe$_2$O$_3$ nanorods electrodes.

	R_θ/Ω	R_f/Ω	R_{ct}/Ω	$W/m\Omega$
α-Fe$_2$O$_3$ nanorods	4.13	13.4	85.3	39.2
α-Fe$_2$O$_3$ nanorods/CNFs	3.92	3.80	30.4	38.1

Fig. 6. Voltage–capacity profiles of bare α-Fe$_2$O$_3$ nanorods (a) and α-Fe$_2$O$_3$ nanorods/CNFs (b) electrodes at 0.2C (200 mA g^{-1}) in the voltage range of 0.005–3.0 V vs. Li$^+$/Li.

discharge capacity and the capacity retention are different. The initial discharge capacity is 1069 mAh g^{-1} for the bare α-Fe$_2$O$_3$ nanorods, but 1278 mAh g^{-1} for the α-Fe$_2$O$_3$ nanorods/CNFs. This value is the same as that of the α-Fe$_2$O$_3$ nanorod array on electrospinning CNFs [19]. After 30 cycles, the discharge capacity remains 560 mAh g^{-1} for the bare α-Fe$_2$O$_3$ nanorods, but 960 mAh g^{-1} for the α-Fe$_2$O$_3$ nanorods/CNFs, compared to the 758 mAh g^{-1} of the α-Fe$_2$O$_3$ nanorod array on electrospinning CNFs after 50 cycles [19]. It is apparent that the introduction of CNFs improves not only the initial discharge capacity but also the cyclic stability of α-Fe$_2$O$_3$. The enwrapping of α-Fe$_2$O$_3$ nanorods by CNFs provides an electronic network, enforcing the electronic contacts among active materials and current collector and thus improving the discharge capacity. On the other hand, the soft and curly CNFs provide bondage and buffer for volume change of α-Fe$_2$O$_3$ nanorods due to lithium ion insertion/de-insertion, preventing the nanostructure from destruction and thus improving the cyclic stability.

To confirm the structure stability of α-Fe$_2$O$_3$ nanorods, SEM observations were performed on the cycled electrodes. As shown in Fig. 7a and b, although particle size becomes larger than that before cycling, the α-Fe$_2$O$_3$ in the composite electrode remains its nanorod morphology after 30 cycles. Differently, after 30 cycles the particles in the bare α-Fe$_2$O$_3$ nanorods electrode inflates dramatically and the nanorod morphology cannot be identified, as shown in Fig. 7c and d. The structure destruction of bare α-Fe$_2$O$_3$ nanorods due to the cycling is responsible for its gradually decrease capacity. By contrast, the introduction of CNFs provides a buffer for the volume change of the α-Fe$_2$O$_3$ nanorods and enhances its structure stability.

Fig. 8 compares the rate performance of the α-Fe$_2$O$_3$ nanorods/CNFs composite with the bare α-Fe$_2$O$_3$ nanorods. Four current rates, 300 mAh g^{-1} (0.3C), 1000 mAh g^{-1} (1C), 2000 mAh g^{-1} (2C), and 12,000 mAh g^{-1} (12C), were considered. The discharge capacity at 30th cycle is 535 mAh g^{-1}, 446 mAh g^{-1}, 317 mAh g^{-1} and 98 mAh g^{-1} for the bare α-Fe$_2$O$_3$ nanorods (Fig. 8a), while improved to 932 mAh g^{-1}, 736 mAh g^{-1}, 530 mAh g^{-1} and 292 mAh g^{-1} for the composite (Fig. 8b), at 0.3C, 1C, 2C, and 12C, respectively. These results confirm that the introduction of CNFs improves the rate discharge capacity of α-Fe$_2$O$_3$ nanorods significantly, showing the contribution of CNFs to the improvement of electronic conductivity of electrode materials and the reduction of charge transfer resistance for lithium insertion/de-insertion. Our α-Fe$_2$O$_3$ nanorods/CNFs composite also exhibit better rate capability than the α-Fe$_2$O$_3$/MWCNTs that delivered 819, 605, 464, and 337 mAh g^{-1} at 100, 200, 500, and 1000 mA g^{-1}, respectively [33], the α-Fe$_2$O$_3$—C nanocomposite that delivered 688 mAh g^{-1} after 50 cycles at 0.2C rate and 370 mAh g^{-1} after 20 cycles at 2C [34], and the α-Fe$_2$O$_3$ nanorod array on electrospinning CNFs that delivered 245 mAh g^{-1} at 10C [19].

4. Conclusions

In this paper, we reported a novel α-Fe$_2$O$_3$/carbon composite as anode of lithium ion battery. α-Fe$_2$O$_3$ nanorods were synthesized by hydrothermal method and the α-Fe$_2$O$_3$ nanorods/CNFs composite was obtained by introducing CNFs during the formation of α-Fe$_2$O$_3$ nanorods. The α-Fe$_2$O$_3$ nanorods are enwrapped with soft and curly CNFs. The enwrapping of α-Fe$_2$O$_3$ nanorods by CNFs provides an electronic network, which enforces the electronic contacts among active materials and current collector and improves the physical contact between electrolyte and electrode, and provides bondage and buffer for volume change of α-Fe$_2$O$_3$ nanorods due to lithium ion insertion/de-insertion. The resulting composite delivers higher discharge capacity and exhibits better cyclic stability and rate capability than the bare α-Fe$_2$O$_3$ nanorods, and thus is a promising anode material for high energy and high power lithium ion batteries.
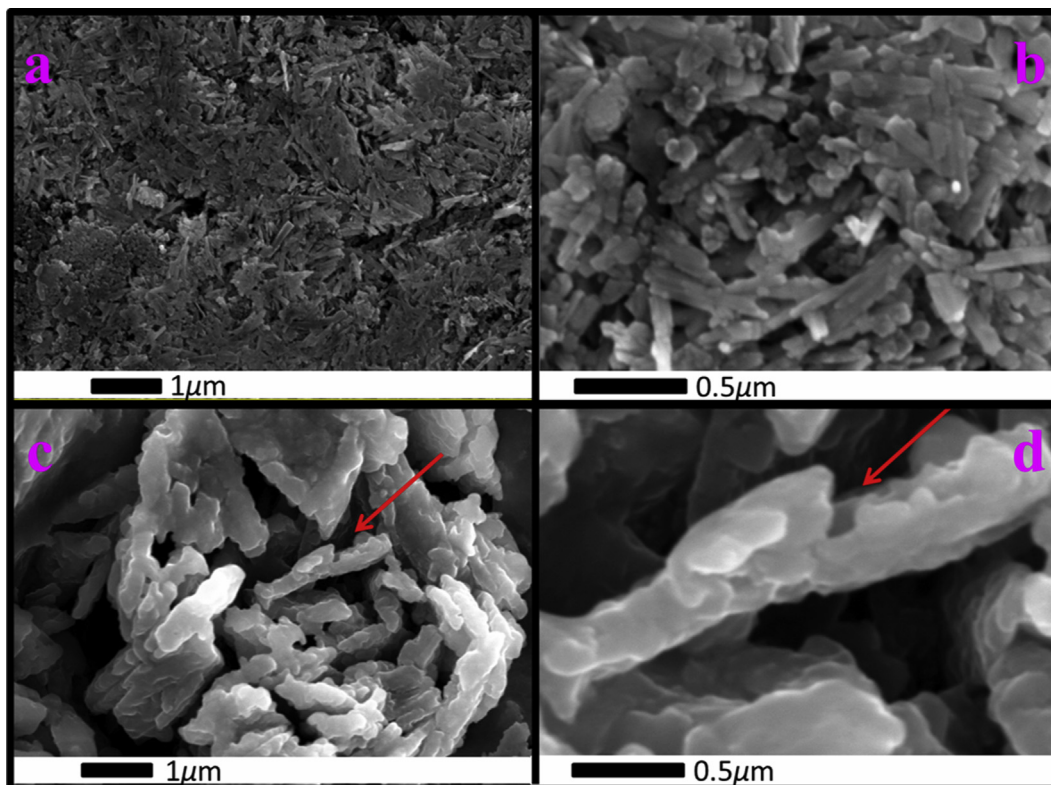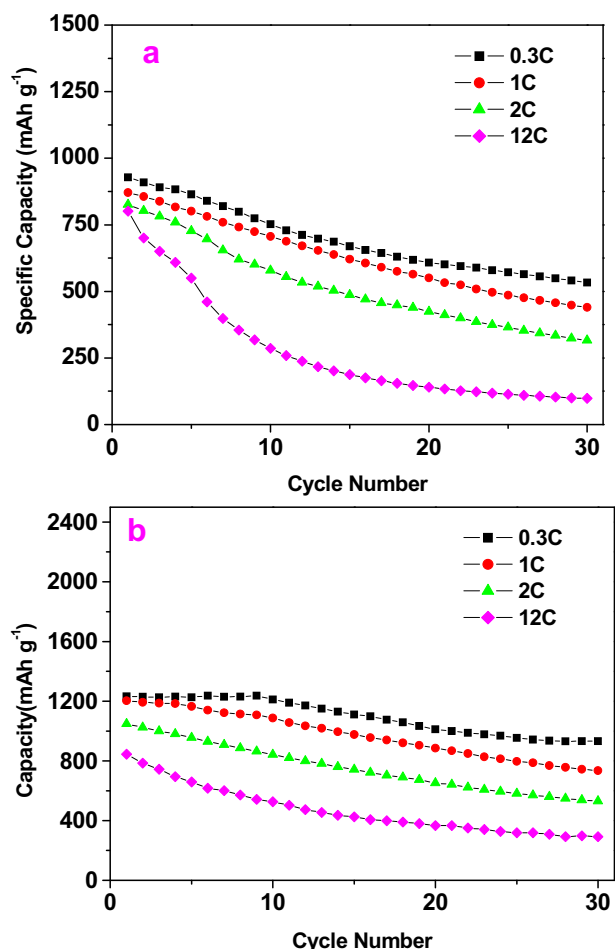

Fig. 7. SEM images of α-Fe$_2$O$_3$ nanorods/CNFs (a, b) and bare α-Fe$_2$O$_3$ nanorods (c, d) electrode after 30 cycles of charging/discharging at 0.2C.

Fig. 8. Cycling performance of bare α-Fe$_2$O$_3$ nanorods (b) and α-Fe$_2$O$_3$ nanorods/CNFs (a) electrodes at different high current densities in the voltage range of 0.005–3.0 V vs. Li$^+$/Li.

References

[1] M. Armand, J.M. Tarascon, Nature 451 (2008) 652–657.
[2] X.D. Xiang, X.Q. Li, W.S. Li, J. Power Sources 230 (2013) 89–95.
[3] M.Q. Xu, Y.L. Liu, B. Li, W.S. Li, X.Q. Li, S.J. Hu, J. Power Sources 18 (2012) 123–126.
[4] J.F. Lei, W.S. Li, X.P. Li, Elton J. Cairnsd, J. Mater. Chem. 22 (2012) 22022–22027.
[5] C.M. Park, H.J. Sohn, Adv. Mater. 22 (2010) 47–52.
[6] E. Kang, Y.S. Jung, A.S. Cavanagh, G.H. Kim, S.M. George, A.C. Dillon, J.K. Kim, J. Lee, Adv. Funct. Mater. 21 (2011) 2430–2438.
[7] Y.S. Jung, S. Lee, D. Ahn, A.C. Dillon, S.H. Lee, J. Power Sources 188 (2009) 286–291.
[8] C.S. Johnson, N. Li, C. Lefief, M.M. Thackeray, Electrochem. Commun. 9 (2007) 787–795.
[9] Z.Y. Wang, L. Zhou, X.W. Lou, Adv. Mater. 24 (2012) 1903–1911.
[10] C. Jia, L. Sun, F. Luo, X. Han, L. Heyderman, Z. Yan, C. Yan, K. Zheng, Z. Zhang, M. Takano, J. Am. Chem. Soc. 130 (2008) 16968–16977.
[11] X.J. Zhu, Y.W. Zhu, S. Murali, M.D. Stoller, R.S. Ruoff, ACS Nano 5 (2011) 3333–3338.
[12] N.Q. Liu, J. Shen, D. Liu, Electrochim. Acta 97 (2013) 271–277.
[13] F. Guo, Y. Ye, Z.X. Yang, C.Y. Hong, L.Q. Hu, C.X. Wu, T.L. Guo, Appl. Surf. Sci. 270 (2013) 621–626.
[14] X.L. Wu, D.Q. Han, S. Huang, Y.S. Li, S. He, M.Z. Zhang, F. Feng, X. Liang, ACS Appl. Mater. Interfaces 5 (2013) 3764–3769.
[15] C.W. Lee, K.N. Lee, J.S. Lee, Mater. Lett. 63 (2009) 2607–2610.
[16] Y.D. Huang, Z.F. Dong, D.Z. Jia, Z.Q. Guo, W. Cho, Solid State Ion. 1 (2011) 54–59.
[17] J. Shao, J.X. Zhang, J.J. Jiang, G.M. Zhou, M.Z. Qu, Electrochim. Acta 56 (2011) 7005–7011.
[18] B. Jang, M. Park, O.B. Chae, S. Park, Y. Kim, S.M. Oh, Y. Piao, T. Hyeon, J. Am. Chem. Soc. 134 (2012) 15010–150105.
[19] Z.L. Liu, S.W. Tay, Mater. Lett. 72 (2012) 74–77.
[20] Z.L. Liu, S.W. Tay, X. Lia, Chem. Commun. 47 (2011) 12473–12475.
[21] L. Taberna, S. Mitra, P. Poizot, P. Simon, J.M. Tarascon, Nat. Mater. 5 (2006) 567–573.
[22] R. Liu, J. Duay, S.B. Lee, Chem. Commun. 47 (2011) 1384–1404.
[23] Y. Zhao, J.X. Li, Y.H. Ding, L.H. Guan, Chem. Commun. 47 (2011) 7416–7418.
[24] S.W. Kim, D.H. Seo, H. Gwon, J. Kim, K. Kang, Adv. Mater. 22 (2010) 5260–5264.
[25] C.L. Li, L. Gu, J.W. Tong, J. Maier, ACS Nano 5 (2011) 2930–2938.
[26] B.C. Jang, M.Y. Park, O.B. Chae, S.J. Park, Y.J. Kim, S.M. Oh, Y.Z. Piao, T.W. Hyeon, J. Am. Chem. Soc. 10 (2012) 1021–1026.
[27] G.M. Zhou, D.W. Wang, F. Li, L.L. Zhang, N. Li, Z.S. Wu, L. Wen, G.Q. Lu, H.M. Cheng, Chem. Mater. 22 (2010) 5306–5313.
[28] S.L. Chou, J.Z. Wang, D. Wexler, K. Konstantinov, C. Zhong, H.K. Liu, S.X. Dou, J. Mater. Chem. 20 (2010) 2092–2908.
[29] P. Poizot, S. Laruelle, S. Grugeon, L. Dupont, J.M. Tarascon, Nature 407 (2000) 496–499.
[30] B. Li, M.Q. Xu, T.T. Li, W.S. Li, S.J. Hu, J. Power Sources 17 (2012) 92–95.
[31] S. Behea, J. Power Sources 196 (2011) 8669–8674.
[32] S.L. Jin, H.G. Deng, X.J. Liu, L. Zhan, X.Y. Liang, W.M. Qiao, L.C. Ling, J. Power Sources 196 (2011) 3887–3893.
[33] Y.D. Huang, Z.F. Dong, D.Z. Jia, Z.P. Guo, W.I. Choe, Solid State Ion. 201 (2011) 54–59.
[34] F. Cheng, K. Huang, S. Liu, J. Liu, R. Deng, Electrochim. Acta 56 (2011) 5593–5598.
[35] J. Hassoun, P. Ochal, S. Panero, G. Mulas, C.B. Minella, B. Scrosati, J. Power Sources 180 (2008) 568–575.